

Antiferromagnetic weak topological state in Bismuth square-net based nonsymmorphic lattice

Prabuddha Kant Mishra,[†] Shivani Kumawat,[‡] Soumyakanta Panda,[¶] Niharika Mohapatra,[¶] B K Mani,[‡] and Ashok Kumar Ganguli^{*,†,§}

[†]*Department of Chemistry, Indian Institute of Technology Delhi, New Delhi 110016, India*

[‡]*Department of Physics, Indian Institute of Technology Delhi, New Delhi 110016, India*

[¶]*School of Basic Sciences, Indian Institute of Technology Bhubaneswar, Odisha 752050, India*

[§]*Department of Chemical Sciences, Indian Institute of Science Education and Research, Berhampur, Odisha-760003, India*

E-mail: ashok@chemistry.iitd.ac.in

Abstract

The ZrSiS-class of layered materials offer interesting topological and magnetic characteristics suitable for spintronics applications. In this work, we have synthesized a polycrystalline NdBiTe using solid-state reaction technique and have examined the magnetic properties in 2 - 300 K temperature range using temperature and field-dependent magnetization measurements. Our magnetic and specific heat data demonstrates a long-range antiferromagnetic ordering in the material below 4.5 K. Furthermore, our isothermal magnetization data show a signature of spin-reorientation below Neel temperature. The observed nonlinearity in inverse susceptibility vs temperature data, and a hump in specific heat in 5-20 K range, indicate the existence of crystal field splitting in the material. Our transport properties measurements show the metallic behavior with positive magnetoresistance in the temperature range of 2 - 300 K. The observed rise in resistivity as function of temperature below Neel temperature infers the strongly correlated fermions, which is consistent with the observed large Sommerfeld coefficient. Consistent with experimental results, our first-principles calculations predict an antiferromagnetic semimetallic nature of Nd-

BiTe. Further, our spin-orbit coupled simulations of electronic structure show a signature of weak topological nature of the material.

Introduction

Systematic understanding of the interplay among topology, magnetism, and electrical properties of materials has been of prime interest for the last few decades. Materials with correlated electronic interactions play a pivotal role in comprehending the mechanistic links and inter-dependency between various degrees of freedom like spin and charge. Rare-earth rich systems are prone to have magnetic interactions due to the presence of *f*-electrons and the properties of such materials are substantially influenced by interactions among conducting electrons and localized moments, termed as RKKY (Ruderman-Kittel-Kasuya-Yosida) interaction. A family of ZrSiS-type structures has been explored for topological and magnetic properties.¹⁻⁶ Layered materials often exhibit crystal-field splittings due to the reduced symmetry arising from stacking along a particular axis. The interlayer and the inter-ligand distances have been found to be crucial to affect the extent of crystal-field

energy splitting. In addition to it, both theoretical and experimental investigations have been performed to reveal the presence of topological properties intricately connected with non-symmorphic layered structures in these materials. The degeneracy of nodal-line in nonsymmorphic materials is protected by crystal symmetry which makes it different from Dirac semimetals and Weyl semimetals.⁷ Such intertwined aspects of structure and topology of the electronic band have been explored for nodal-line semimetal ZrSiX ($X = \text{S, Se, and Te}$) by ARPES (angle-resolved photoemission spectroscopy) and magnetotransport measurements.⁸⁻¹⁴

The materials consisting of the square-net like structures have been investigated to have symmetry-protected four-fold Dirac states in Brillouin zone.^{15,16} The theoretical predictions identified LaSbTe, a nonmagnetic material, as a potential weak topological insulator due to its significant spin-orbit coupling.¹⁷ Subsequent experimental validation confirmed the presence of a Dirac-like dispersion within its electronic band structure.¹⁸ In the case of magnetic isostructural analogues, magnetism is an additional tuning parameter to be explored. Non-trivial topological phase in long-range antiferromagnetically ordered materials has been observed through both experiments as well as first-principles simulations. Experimentally it was observed in ARPES measurement in GdSbTe¹⁹ and CeSbTe,⁷ whereas theoretically it was reported in HoSbTe.⁶ Diverse magnetic features like devil's staircase and spin-flop transitions have been observed in various members of LnSbTe (Ln = rare earth). Moreover, the coexistence of competitive short-range magnetism and long-range ordering has been explored in HoSbTe, TbSbTe²⁰ and CeSbTe³ materials. Interestingly, the antiferromagnetically ordered magnetic moments exhibit a change in their orientations relative to the square lattice arrangements of the rare-earth elements in ZrSiS materials. This suggests a change in the interatomic exchange interaction, allowing a tunable single-ion anisotropy. Though ZrSiS-class of LnSbTe are known and have been studied for physical properties, Bi-square net based ZrSiS-

type of materials are still unexplored. Such materials are however important as they exhibit exotic fundamental as well as functional properties due to their larger atomic radii and stronger spin-orbit coupling compared to their Sb-analogues.

In this study, we have successfully synthesized the polycrystalline NdBiTe, a new member of the ZrSiS family, by solid-state reaction technique. NdBiTe is a bismuth-based layered magnetic material, which requires a focused attention to comprehensively investigate the interplay among magnetism, nontrivial topological characteristics, and transport properties. Detailed magnetic measurements have been carried out to explore the nature of various interactions. With the help of temperature-dependent and isothermal magnetic measurements, our study found a robust long-rang antiferro-type magnetic ordering in NdBiTe. Furthermore, the field-dependent specific heat studies infer details of thermal parameters and establish it as a strongly correlated electronic system. Due to the effect of strongly correlated electrons, resistivity rises below Neel temperature. The observed nontrivial field dependence of MR reveals its genesis from the nontrivial topology of the electronic band structure. In addition, to support our experimental results, we performed first-principles density functional theory calculations of the relevant properties in NdBiTe. Our computed results are consistent with our measured values.

The remainder of the paper is organized in two sections. In Section II, we provide brief details on experimental and computational methods used in the work. In Section III, we discuss and analyze the results from our experiment and calculations. For an easy discussion, we have separated this section in to five subsections.

Experimental and Computational Details

Polycrystalline NdBiTe has been synthesized by solid-state reaction method using a sealed tube technique. The elemental form of Nd, Bi, and

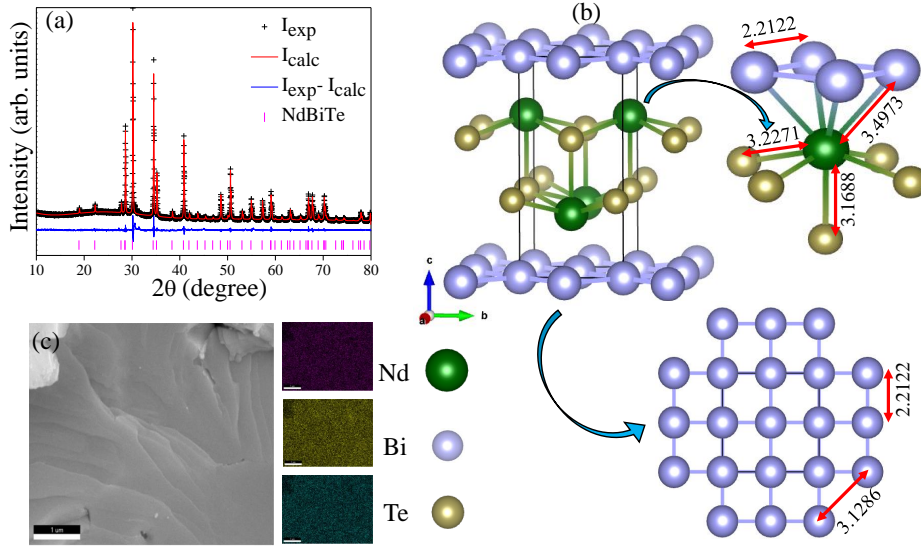


Figure 1: (Color online) (a) Rietveld refinement of room temperature powder X-ray diffraction data of polycrystalline NdBiTe. Vertical bars show the allowed Bragg's peak for NdBiTe. The blue line represents the difference in the experimental and simulated patterns. (b) Shows the Crystal structure of NdBiTe, with constituents of polyhedra around Nd ion and the square-net layer of Bismuth, mentioned with various interatomic distances in Å unit. (c) The SEM image shows the layered nature of the specimen along with elemental mapping to show the homogeneous distribution of elements.

Te have been ground together in the stoichiometric ratio (Nd:Bi:Te::1:1:1) in an argon-filled glove box and sealed in an evacuated quartz tube for heat treatment in a programmed high-temperature furnace. A heating condition of 973 K for 48 hours was used for the reaction. The product of the first heating was ground well, pelletized, and sintered at 973 K for 48 hours for better phase homogeneity. Resulting phases have been characterized using X-ray diffraction technique using Bruker D8 Advance diffractometer with Cu-K α radiation performed on powder, shown in Fig. 1. The structural refinement on powder X-ray diffraction data was carried out using the Rietveld method with the TOPAS software package. By using the EDX (energy dispersive X-ray analysis) technique, we confirmed the homogeneity and composition of the sample. The temperature and field-dependent magnetic measurements were performed in a superconducting quantum interference device (MPMS-3). The specific heat and electrical transport were measured as a function of temperature and applied field by using physical property measurement system (PPMS,

Quantum Design).

To support our experimental results, we performed density functional theory (DFT) based first-principles calculations using the projected augmented wave (PAW) method²¹ as implemented in the *Vienna Ab initio Simulation Package* (VASP) code.^{22–24} The exchange-correlations among electrons were incorporated using the generalized gradient approximation (GGA) based Perdew-Burke-Ernzerhof (PBE) pseudopotential.²⁵ The plane-wave basis with an energy cutoff of 500 eV were used in all the calculations. The crystal structures were optimized using full relaxation calculations with the help of a conjugate gradient algorithm with a Γ -centered k grid of $10 \times 10 \times 4$. The energy and force convergence criteria of 10^{-6} and 10^{-5} eV, respectively, are used in all the self-consistent-field calculations. To incorporate the effect of strongly correlated $4f$ -electrons of Nd, on-site Coulomb interaction was included using the rotationally invariant DFT+U approach of Dudarev et al.^{26,27} Our calculated U value, 6.58 eV, is consistent with the previous calculations for similar systems.²⁸ Further, to incorporate

Table 1: Structural and magnetic parameters of NdBiTe in their respective units.

Space group:	$P4/nmm$				
Space group number:	129				
a (Å):	4.4245(1)				
c (Å):	9.3775(2)				
Atom	Site	x	y	z	B_{iso}
Nd	2c	0	1/2	0.2889(3)	1.13(6)
Bi	2a	0	0	0	1.33(5)
Te	2c	0	1/2	0.6268(3)	2.19(7)
T_N					4.5(1) K
Θ_P					-18.78(5) K
C					1.652(2) emu Oe ⁻¹ mol ⁻¹ K ⁻¹
$\chi(0)$					0.00133 emu Oe ⁻¹ mol ⁻¹
$\mu_{\text{eff}}^{\text{theo}}$					3.63 μ_B /Nd ⁺³
$\mu_{\text{eff}}^{\text{calc}}$					3.68(5) μ_B /Nd ⁺³
$M_S(2K)$					1.16(2) μ_B mol ⁻¹
$H_C(2K)$					45(5) Oe

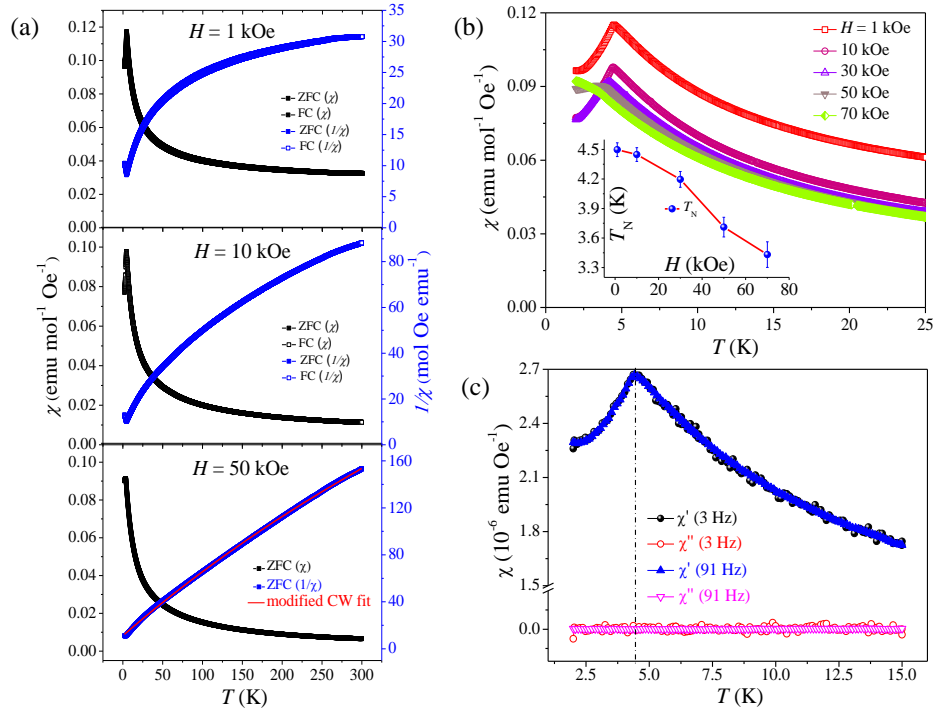


Figure 2: (Color online) (a) Magnetic susceptibility ($\chi(T)$) and corresponding inverse susceptibility ($\chi^{-1}(T)$) in zero-field-cooling (ZFC) and field-cooling (FC) at different fields (1, 10 and 50 kOe). $\chi^{-1}(T)$ at the applied field of 50 kOe, fitted with modified C-W model, shown by red solid line. (b) Variation of ZFC $\chi(T)$ at various applied magnetic fields in low-temperature regime (2-25 K), the inset shows the suppression of T_N as a function of the applied field. (c) The χ' and χ'' components of ac-susceptibility data in the temperature range of 2-15 K at 3 and 91 Hz frequencies.

the relativistic effects, arising from the heavier atoms Bi and Nd, we included spin-orbit coupling (SOC) in all the calculations. A supercell of $2 \times 2 \times 2$ (48 atoms) was used to calculate the phonon dispersion and other relevant properties. The phonon dispersions were calculated with Γ -centered k -mesh of $3 \times 3 \times 2$ using linear response density functional perturbation theory (DFPT) as implemented in PHONOPY.^{29,30}

RESULTS AND DISCUSSION

Fig. 1(a) shows the Rietveld refinement of room temperature powder X-ray diffraction pattern of NdBiTe. It crystallizes in the ZrSiS-type centrosymmetric tetragonal structure with space group $P4/nmm$ and the lattice parameters are $a = 4.4245(1)$ Å and $c = 9.3775(2)$ Å. The details of refined structural parameters are given in Table 1. Fig. 1(b) shows the crystal structure of NdBiTe, where Nd and Te ions occupy the 2a sites while 2c sites are filled with Bi, and each Nd-ion is coordinated by *five* Te ions and *four* Bi ions. The polyhedral structure around Nd can be seen as a square antiprismatic geometry. This geometry will lead to anisotropic magnetism and crystal-field energy splitting for otherwise degenerate Nd-f electrons. Like other ZrSiS materials, NdBiTe can be visualized as the stacking of two distinct layered components [NdTe] and Bi. The interatomic interaction will be helpful in deciding the effective bonding among these for compound formation. In earlier reports, the c/a ratio is used for comprehension of the nature of bonding in layered materials.¹⁵ For NdBiTe, the c/a is 2.12, which is close to that of GdBiTe ($c/a = 2.11$). Thus NdBiTe belong to same structural class of ZrSiS type ($c/a = 2.27$) layered materials having ionic interaction among adjacent layers.²⁸ The delocalized bonding in the square-net of Bi is key to transport properties and stabilizes the square-net geometry.^{7,15,16} The intraplanar Bi-Bi bond length is found to be shorter in NdBiTe (3.129 Å) as comparable to its structural analogue GdBiTe (3.0905 Å). Here, it is important to mention that the observed Bi-Bi bond

length is comparable to the puckered honeycomb units in the elemental form of bismuth (3.071 Å).³¹ In [NdTe] layer, two distinct Nd-Te bond lengths are observed as shown in the Fig. 1(b). The four in-plane (\parallel ab plane) Nd-Te bonds are longer (3.227 Å) than one out-of-plane Nd-Te bond (3.169 Å) i.e. \parallel to c-axis.

Temperature Dependent Magnetic Susceptibility

Fig. 2(a) shows the temperature-dependent magnetization measurements where we have shown our data on χ (T) at different applied fields along with inverse susceptibility in the temperature range of 2-300 K, measured in both zero-field-cooled (ZFC) and field-cooled (FC) protocols. As discernible from the panel (a), the $\chi(T)$ data with ZFC and FC protocols overlap with each other. This suggests the absence of irreversibility through competing magnetic interactions or glassy-spin nature in the material.³² The magnetization increases with a decrease in the temperature up to the Neel temperature ($T_N = 5$ K) and below T_N it decreases due to the antiferromagnetic (AFM) alignment of the magnetic spins. The inverse susceptibility versus temperature data show a significant deviation from the linear behavior and does not follow the Curie-Weiss (C-W) law for a larger range of low temperatures. The reason for this nonlinear behavior of χ^{-1} vs T could be attributed to the crystal field splitting of the energy levels, which gets suppressed gradually as the applied field increases from 1 kOe to 50 kOe. A similar trend of deviation from C-W fit below 150 K is reported in a single crystal of CeSbTe.³ From the modified C-W fit, C is estimated to be 1.652 (2) emu K Oe⁻¹ mol⁻¹ and θ_p (Weiss-temperature) is obtained as -18.78 K, which suggests an antiferromagnetic-type exchange interactions between the spins. The χ_0 was estimated to be 0.00133(1) emu Oe⁻¹ mol⁻¹, which was used further to calculate the effective magnetic moments (μ_{eff}) of the material. The μ_{eff} was extracted to be $3.635 \mu_B/\text{Nd}^{+3}$ ions, which is consistent with theoretical value ($g\sqrt{J(J+1)}\mu_B$) $3.63 \mu_B/\text{Nd}^{+3}$.

Next, as the sharpness of transition at T_N de-

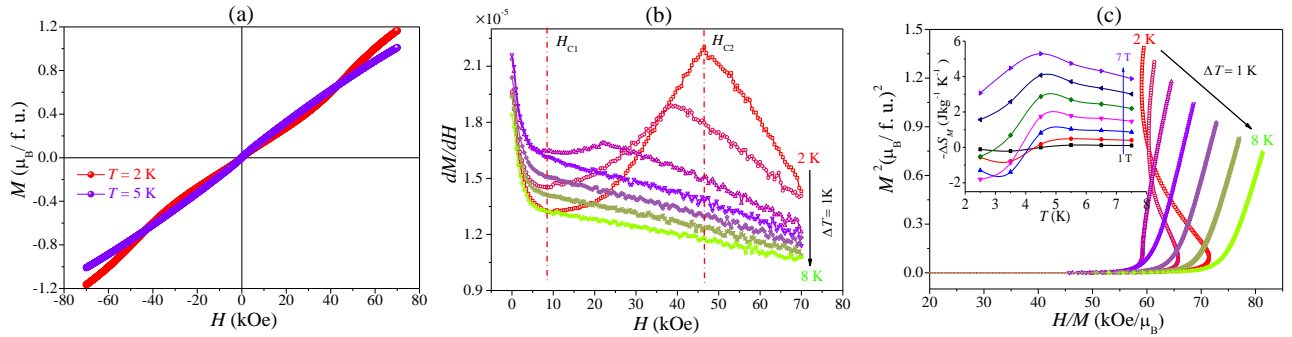


Figure 3: (Color online) (a) Isothermal magnetization (MH) data as a function of applied magnetic field at 2 and 5 K. (b) dM/dH as a function of applied magnetic field at various temperatures across the magnetic transition from 2 K to 8 K, with $\Delta T = 1$ K. The dotted red lines show the critical fields (H_{C1} and H_{C2}) for 2 K curve, as a case of representation. (c) The corresponding Arrott plots and inset demonstrates the change in entropy of magnetization as a function of temperature for various fields ranging from 10 kOe to 70 kOe.

creases with increase in the applied field, we carried out the first derivative of $\chi(T)$ at different fields with respect to temperature to determine the Neel temperature. As can be observed from the panel (b) of the figure, the paramagnetic (PM) to AFM transition is robust for applied external magnetic fields and the T_N is found to decrease gradually with an increase in the field strengths, eventually reaching to ≈ 3.4 K for $H = 70$ kOe (inset of Fig. 2(b)). It is worth mentioning that the AFM long-range orderings have been observed for the isostructural magnetic materials with rare-earth elements.^{1,2} Furthermore, to resolve the possibility of the existence of glassy spin interaction at low-temperature regime, *ac*-susceptibility measurements were performed at 3 and 91 Hz frequencies. As discernible from the Fig. 2(c), the *ac*-susceptibility data show a peak-shaped anomaly close to 4.48 K (T_f) for the in-phase component of susceptibility (χ'), with no signature of frequency dependent behavior. In addition, the out-of-phase component (χ'') shows no significant change as a function of temperature, which suggests the absence of spin-glass-like short range interactions.

Isothermal Magnetization

Next, we performed isothermal $M(H)$ measurements to probe magnetization in the vicinity of

T_N , as shown in Fig. 3. As discernible from the panel (a), $M - H$ loops are consistent with the antiferromagnetic nature of NdBiTe below T_N . The $M(H)$ data at 2 K has a change in the slope with an increase in the magnetic field, suggesting a spin-reorientation in the material. The change in the slope of M_H curves is more visible in the dM/dH plots shown in panel (b)) at various temperatures. There are two points of inflection in the dM/dH vs H data, denoted as H_{C1} and H_{C2} to represent the corresponding critical fields for spin reorientation. As can be observed from the figure, the H_{C2} decreases gradually from 46.5 kOe to 21.5 kOe with an increase in the temperature from 2 K to 4 K, and eventually disappears above the T_N . This suggests the weakening of the antiferromagnetic interaction among spins with increase in the temperature. Contrary to H_{C2} , there is no significant change in H_{C1} with temperature. The change in the slope with magnetic fields suggests a transition from AFM state to a canted-AFM state, where the canting of spins leads to a deviation from the linearity in isotherms and adds a ferromagnetic-like response in the magnetization data. The presence of spin-reorientation-driven metamagnetic transitions in isothermal magnetization at low temperatures is also observed in other isostructural materials with AFM ordering.^{2,5,7,33,34} The saturation magnetization observed from our exper-

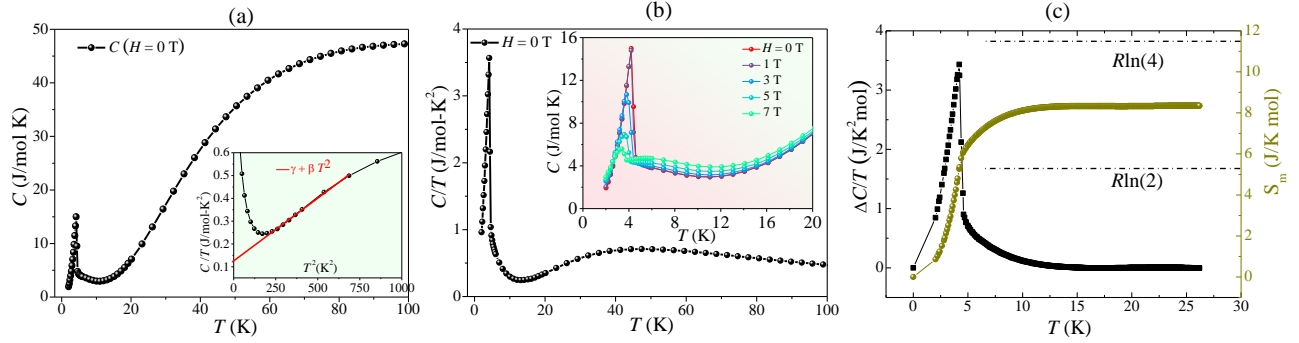


Figure 4: (Color online) (a) The specific heat data as a function of temperature in the absence of applied magnetic field. The inset shows C/T vs. T^2 plot fit (solid red line) with equation $\gamma + \beta T^2$. (b) C/T vs. T plot signifying the peak centered at ~ 48 K, corresponding to Schottky anomaly. The inset shows a temperature-dependent specific heat at various applied magnetic fields.

iment is $1.18 \mu_B/\text{Nd}^{+3}$ at 2 K with an applied field of 7 T. This is comparable to the observed average value of magnetization for NdSbTe by Pandey et al. ($1\mu_B/\text{Nd}^{+3}$),² and Sankar et al. ($1.25\mu_B/\text{Nd}^{+3}$).¹ The relatively large value obtained by Sankar et al., has been attributed to anisotropic magnetization. The observed value of saturation magnetization is smaller in comparison to the theoretical value $3.27 \mu_B/\text{Nd}^{+3}$, indicating the presence of appreciable single-ion anisotropy.^{1,35} Next, we used the virgin plots, recorded at various temperatures around the T_N , to extract the Arrott plot. This is shown in the panel (c) of the figure. The negative slope of curves in the Arrott plot suggests the first order of phase transition to AFM state, supported by Banerjee criterion.³⁶

Further, the change in the magnetization entropy, ΔS_M , associated with the magnetic transition was obtained from the pyromagnetic coefficient $\frac{\partial M(T,H)}{\partial T}$ using the relation

$$\Delta S(T, H_0) = \int_0^{H_0} \left[\frac{\partial M(T, H)}{\partial T} \right]_H dH. \quad (1)$$

The ΔS_M as a function of temperature at various magnetic fields is shown in the inset of Fig. 3 (c). As can be observed from the data, it resembles the $M(T)$ behavior from dc susceptibility Fig. 1(a). ΔS_M acquires a positive value at low applied field (0.1 T), suggesting the presence of antiferromagnetic interaction at low fields. The sign of ΔS_M gradually changes from

positive to negative with increasing magnetic field strengths. The negative value indicates the spin-reorientation for higher applied fields and has a maximum value $\approx -5.15 \text{ J kg}^{-1}\text{K}^{-1}$ at 4.5 K for $\Delta H = 7$ T.

Specific Heat

To gain further insights into the magnetic interactions embedded in antiferromagnetic ordering at low temperatures, we performed specific heat measurements at various applied magnetic fields. Fig. 4(a) shows the specific heat data in the absence of applied magnetic field over a range of temperatures. As discernible from the figure, we observed an anomaly at 4.5 K, confirming a long-range magnetic ordering. This is consistent with the temperature-dependent susceptibility behavior shown in Fig. 2. The field-dependent specific heat data from our measurement are shown in the inset of Fig. 4(b). As can be observed from the figure, the intensity of the anomaly decreases, and also shifts to lower temperatures, with increase in the strengths of applied magnetic field. This is a signature of an antiferromagnetic interaction.

Since our measured specific heat data embeds the contributions from electronic, lattice, and magnetic interactions, to assess their individual contributions we fit the data with temperature-dependent specific heat equation, in the low-

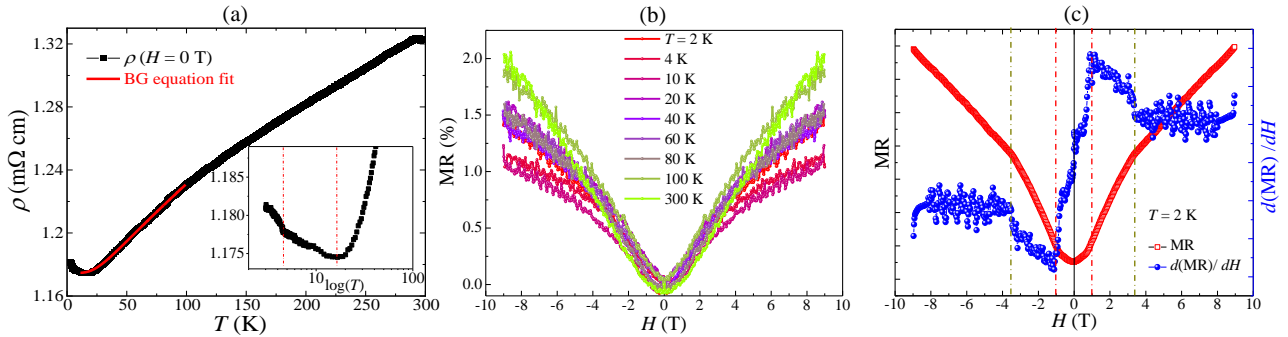


Figure 5: (Color online) (a) Temperature-dependent resistivity $\rho(T)$ in 2 - 300 K range. The solid red line shows a fit to BG equation in the high-temperature regime. The inset shows $\rho(T)$ data in logarithmic scale, where the dotted red lines represent an upturn in $\rho(T)$ at ≈ 16 K and a slope change at T_N . (b) The MR data as a function of H at different temperatures. (c) The smoothed MR data as function of H and its first derivative with respect to the applied field. The dotted lines indicate the critical fields.

temperature regime, as

$$C = \gamma T + \beta T^3 + C_m. \quad (2)$$

Here, γ and β are the Sommerfeld and phonon coefficients, respectively, and C_m is the magnetic contribution to the specific heat. The data well above T_N , in the range of 18-26 K, can be fit without considering magnetic contribution.^{3,5} The C/T vs T^2 data shows a linear fit (shown with a solid red line in the inset of panel (a)), with the parameters γ and β estimated to be 126(4) mJ/K² mol and 0.55(1) mJ/K⁴mol, respectively. The relatively larger value of Sommerfeld coefficient as compared to isostructural antiferromagnets (e.g., 115 mJ/K² mol for NdSbTe)² and much larger as compared to nonmagnetic materials (e.g., 2.19 and 0.51 mJ/K² mol for LaSbSe and LaSbTe, respectively³⁷), suggests strong electronic correlations in NdBiTe due to the presence of Nd-4*f*-electrons. There is a possibility of correlated fermionic behavior, resulting in the mass enhancement of fermions. This is consistent with the findings reported in other isostructural magnetic systems.²

The value of phonon coefficient, β , was used further to estimate the Debye temperature using the relation $\theta_D = (12\pi^4 NR/5\beta)^{1/3}$, where $N = 3$ for NdBiTe and R is the universal gas constant. The estimated value of $\theta_D = 147(1)$ K for NdBiTe is lower than that of NdSbTe

($\theta_D = 236$ K by Pandey et al² and 153 K by Sankar et al¹), indicating weaker interatomic interactions present in NdBiTe as compared to NdSbTe. Moreover, a significant hump in the specific heat data in the temperature range of 5-15 K could be attributed to the Zeeman splitting.¹ The observed broader peak in Cp/T versus T data, centered at 48 K, (Fig. 4(b)) indicates a Schottky anomaly due to the crystal-field splitting, similar to observed in NdSbTe.¹ The specific heat can be associated with an entropy change in the magnetic phase transition. This change in the entropy can be obtained by integrating $\Delta C/T$ over a temperature range, where ΔC is the experimental specific heat except the phonon contributions.³⁸ As discernible from Fig. 4(c), the entropy attains a value of ≈ 8.34 J/K mol, slightly lower than the theoretical value of 11.52 J/K mol. The reason for this small difference could be due to the approximate analysis and an error associated with entropy calculation in milikelvin range. A similar trend in entropy is also observed in NdSbTe² and GdSbTe³⁹ materials.

Transport and Magnetotransport Properties

Next, we examined the transport and magnetotransport properties in NdBiTe. For this, we performed the temperature-dependent resistiv-

ity, $\rho(T)$, measurement for polycrystalline pellet of NdBiTe using the standard four-probe method in the temperature range of 2 - 300 K. The data from our measurement is shown in Fig. 5. As discernible from the panel (a) of the figure, consistent with the metallic behavior, ρ decreases linearly with a decrease in the temperature in the range $20 \text{ K} < T < 300 \text{ K}$. However, ρ is found to increase with further decrease in temperature below 20 K and it could be attributed to either Kondo-like behaviour⁴⁰ or electron-electron interaction.⁴¹ The observed positive magnetoresistance implies that the rise in resistivity originate from electron-electron interaction. Similar upturn in resistivity at low temperature was observed in GdBiTe.²⁸ The presence of magnetic interactions well above the T_N observed in the heat capacity data could be corroborated with the minima in the $\rho(T)$. Similar metallic nature is reported in the case of nonmagnetic LaSbTe,¹⁸ and magnetic GdBiTe,²⁸ whereas, other isostructural analogues of early lanthanides $\text{Ln} = \text{CeSbTe},$ ³³ NdSbTe^2 and SmSbTe^42 are reported to show nonmetallic temperature dependence. In addition, nonmonotonic temperature dependence of resistivity is reported in HoSbTe⁶ and DySbTe⁵ systems.

The residual resistivity ratio ($\text{RRR} = R_{300\text{K}}/R_{20\text{K}}$) extracted from our measurements is 1.12. Such a small value suggests the significant scattering of conducting electrons, which is consistent with the other magnetic isostructural analogs with metallic behavior in resistivity data.²⁸ Whereas, the nonmagnetic analogues like LaSbTe¹⁸ and ZrSiS^{13,43} are reported to have significantly larger RRR values. The $\rho(T)$ shows linear temperature dependence in the range of 100-300 K and changes its slope at lower temperatures, which can be analyzed more closely to get information about the phonon scattering. For this, we fit $\rho(T)$ data with the Bloch-Gruneisen equation for acoustic electron-phonon scattering, in the

temperature range (20-100 K), as

$$\rho(T) = \rho(T_0) + A \left(\frac{T}{\Theta_R} \right)^5 \int_0^{\Theta_R/T} \left[\frac{x^5}{(e^x - 1)(1 - e^{-x})} \right] dx. \quad (3)$$

Here, $\rho(T_0)$ is residual resistivity, the parameter A is a pre-factor which depends on the electron-phonon coupling strength, and Θ_R is the Debye temperature derived from resistivity data. From the fit, we obtained the value of A to be $1.17(2) \times 10^{-4}$ and Θ_R is extracted to be $150 \pm 2 \text{ K}$, which is close to the Θ_D obtained from specific heat measurement over the same temperature range.⁴⁴

Further, to explore more about the charge carriers and transport mechanisms, magneto-transport data were recorded at various temperatures in the presence of magnetic field of $\pm 90 \text{ kOe}$, applied perpendicular to the current direction. The magnetoresistance has been calculated from the relation $\text{MR}(\%) = \frac{R(H) - R(0)}{R(0)} \times 100$, where $R(H)$ and $R(0)$ are resistance at finite applied field and zero field. As discernible from Fig. 5(b), positive magnetoresistance were observed for all the measured temperatures. The magnitudes of MR were found to lie in the range of 1 to 2%. The relatively lower MR values at low temperatures infer interacting fermions having less mobility, as observed in other AFM lattices.³² Consistent with our data, similar low values for MR were observed in LaSbSe³⁷ and GdBiTe.²⁸ The symmetrical MR shows a change in slope at two applied fields H_1 and H_2 . As can be observed from the panel (c) of the figure, MR and corresponding $d(\text{MR})/dH$ at 2 K have critical fields as 10 kOe and 34.5 kOe. As the temperature increases, the lower critical field, which is related to the ordered magnetic state, disappears. The $d(\text{MR})/dH$ for all temperatures are given in the supplementary material. Further, the correlated nature of electrons in NdBiTe can be parameterized with the calculation of the Wilson ratio, which is expressed in terms of the low-temperature magnetic susceptibility and Sommerfeld coefficient, as $R_w = \frac{\pi^2 k_B^2 \chi}{\mu_{\text{eff}}^2 \gamma}$, where k_B

is Boltzmann constant, χ represents magnetic susceptibility, μ_{eff} is effective magnetic moment, and γ is the Sommerfeld coefficient. The obtained Wilson ratio is ≈ 12.6 . Such a large value corroborates with correlated fermionic behavior and might have originated from the crystal field splitting of the f -states.

First-Principles Calculations

Next, to support our experimental data, we performed density functional theory based first-principles calculations of the relevant properties in NdBiTe. We start with the structural optimization to achieve the actual ground state of the system. Our optimized lattice parameters, $a = b = 4.467 \text{ \AA}$ and $c = 9.589 \text{ \AA}$, are in good agreement with the experimental values, $a = 4.424 \text{ \AA}$ and $c = 9.377 \text{ \AA}$. The optimized unit cell is slightly elongated. And, the reason for this could be attributed to the use of GGA pseudopotential in our calculations, which is known to overestimate the lattice parameters.⁴⁵

The optimized structure is then used to calculate and examine the electronic structure of the material. In Fig. 6, we have shown our calculated data for density of states (DOS) and bands for the ground state of NdBiTe. As discernible from the figure, our calculated data reveals that the NdBiTe is semimetallic in nature. This is consistent with the semimetallic nature observed in our experiment as well as reported nature in the case of GdSbTe,^{19,39} GdBiTe,²⁸ NdSbTe,¹ and other materials of the ZrSiS family.^{42,46} In panels (a) and (b) of the figure, we have shown our data on total DOS and atom-projected DOS, without and with spin-orbit coupling (SOC), respectively. As discernible from the DOS, the dominant contributions to valence band mainly come from the p -electrons of Bi and Te. Apart from these, Nd also has a significant contribution, where d - and f -electrons contribute the most. Considering the conduction band, it is mainly dominated by Nd- f electrons, specially in the energy range above 0.5 eV.

Next, we examined the magnetic properties of NdBiTe using first-principles calculations. First, to obtain the actual ground state

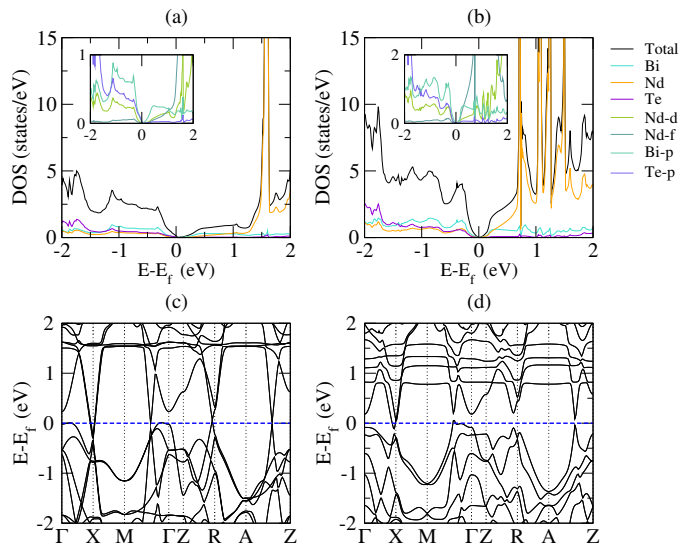


Figure 6: The density of states and atom-projected density of states (a) without and (b) with spin-orbit coupling. Insets in panels (a) and (b) represent the orbital resolved density of states. The electronic band structure of NdBiTe (c) GGA+U (d) GGA+U+SOC. The Fermi level is set to zero.

magnetic configuration of NdBiTe, we probed both ferromagnetic (FM) and antiferromagnetic (AFM) orientations of the magnetic moments. For AFM, there could be two possible spin configurations – an interlayer AFM with intralayer FM (Fig. 7(c)), and an interlayer FM with intralayer AFM (Fig. 7(b)). In Table 2, we have listed the total energies for ferromagnetic and antiferromagnetic AFM-A with respect to the antiferromagnetic AFM-I configuration. As evident from the table, the prefer-

Table 2: Calculated total energy (in meV) of FM and AFM-A configurations relative to that of AFM-I configuration, and the magnetic moments (in μ_B) of the constituent atoms.

$E_{\text{AFM-I}}$	0
E_{FM}	-35.98
$E_{\text{AFM-A}}$	-12.69
μ^{Nd}	3.059
μ^{Bi}	-0.001
μ^{Te}	-0.019
$E_{\parallel} - E_{\perp}$	0.89

able ground state magnetic configuration of NdBiTe is AFM-I, as FM and AFM-A energies are larger by ≈ 35 and 13 meV, respectively. Our calculation is consistent with our experiment and also the literature²⁸ where a similar isostructural material GdBiTe is reported to have AFM-I²⁸ as the ground state. It is to be also mentioned that GdSbTe³⁹ is reported to show an AFM-A magnetic phase. This implies the importance of interplay between SOC, magnetism, and topological degrees of freedom in these materials. In the table, we have also listed the magnetic moment of individual elements. As evident, the dominant contribution is from the Nd ion, and the reason for this is attributed to the unpaired f -electrons. As discernible from the octahedral filling of f -orbital (Fig. 7)(d), the lowest energy state (t_{1g}) is occupied by three majority spins, whereas the high energy states (t_{2g} and a_{2g}) are completely unfilled, leading to three unpaired electrons. Our calculated magnetic moment of Nd is $3.06 \mu_B$ per atom, which is consistent with our measured value of $3.64 \mu_B$. As expected, elements Bi and Te have negligible magnetic moments. Next, to identify the actual direction of spin orientation, we computed the magnetocrystalline anisotropy energy (MAE) in NdBiTe. For this, we considered three principal spin quantization axes, the out-of-plane [001] and the in-plane [100] and [010]. The MAE energy is extracted from the total energies of in-plane and out-of-plane magnetic configurations using $E_{\text{MAE}} = E_{\text{in-plane}} - E_{\text{out-of-plane}}$. The obtained positive E_{MAE} value, 0.89 meV, indicates that NdBiTe prefers an in-plane spin alignment. This is consistent with the previously reported E_{MAE} in GdSbTe.³⁹

The ZrSiS-class of materials have a glide-plane perpendicular to a 4-fold axis of rotation as a symmetry element due to nonsymmorphic crystalline structure. This symmetry facilitates band folding, resulting in band-crossing and, thus, nontrivial topology in the material. Considering this, next we examine the topological features in NdBiTe. For this, we zoom-in the bands at high-symmetry point R and in Fig 8 show the enlarge view of bands for four different cases. As can be observed from panel

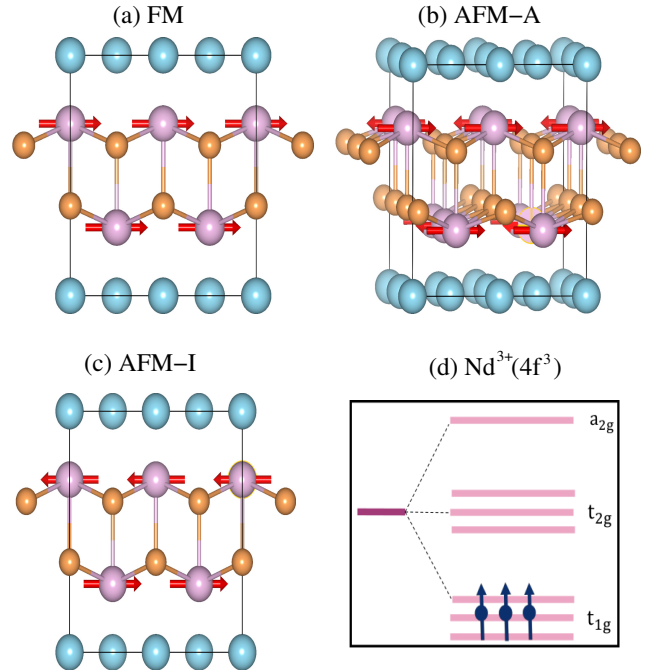


Figure 7: The schematic of (a) FM, (b) AFM-A and (c) AFM-I magnetic configurations. The panel (d) represents the octahedral filling of electrons in f -state of Nd ion.

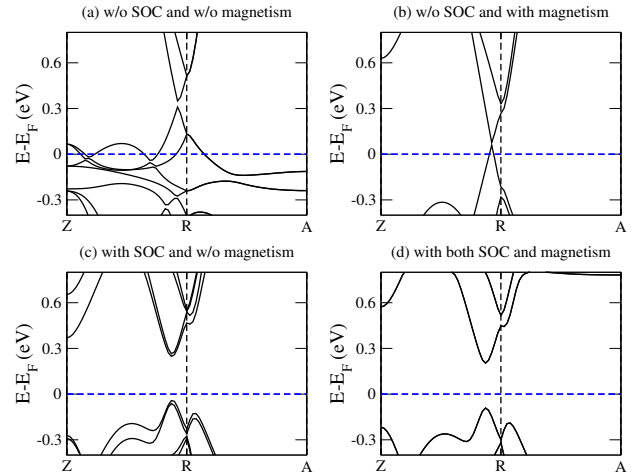


Figure 8: The enlarged view of electronic structure of NdBiTe at high symmetry point R for (a) without SOC and magnetism, (b) without SOC and with magnetism, (c) with SOC and without magnetism, and (b) with SOC and magnetism.

(a), in absence of SOC and magnetic degrees of freedom, the electronic structure of NdBiTe resembles a conventional ZrSiS behavior. However, when the magnetic degrees of freedom is switched on, with AFM-I magnetic spin orien-

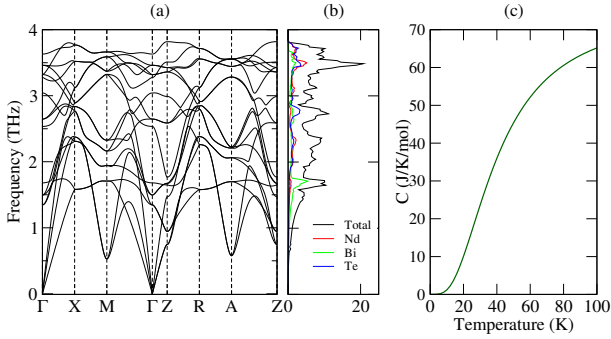


Figure 9: The calculated (a) phonon dispersion (b) phonon density of states and (c) Temperature dependence of specific heat at constant volume for NdBiTe.

tation, we observed band crossings, leading to nodal lines and nodal surfaces, along the high symmetry directions in the Brillouin zone (Fig. 6(c)). The enlarged view of one such crossing is shown in Fig. 8(b) at high-symmetry point R. And, as discernible from panel (c), when the SOC is switched-on in absence of magnetic degrees of freedom, the nodal lines and nodal surfaces break apart, leading to the formation of degenerate Dirac points protected by time-reversal symmetry. In presence of both SOC and magnetism, an opening of bands is introduced in the material (panel (d)). A similar trend of gap openings in presence of SOC were reported recently in HoSbTe,⁶ DySbTe,⁵ GdBiTe,²⁸ CeBiTe, and LaBiTe^{47,48} ZrSiS class of materials. Such behavior of electronic structure is associated with a weak topological nature of the material.

Next, we present and discuss our simulation results on phonon dispersion and specific heat in NdBiTe. The phonons were obtained by solving the equation (as implemented in the Phonopy⁴⁹)

$$\sum_{\beta\tau'} D_{\tau\tau'}^{\alpha\beta}(\mathbf{q})\gamma_{\mathbf{q}j}^{\beta\tau'} = \omega_{\mathbf{q}j}^2\gamma_{\mathbf{q}j}^{\alpha\tau}, \quad (4)$$

where the indices τ, τ' represent the atoms, α, β are the Cartesian coordinates, \mathbf{q} is a wave vector and j is a band index. $D(\mathbf{q})$ refers to as the dynamical matrix, and ω and γ are the corresponding phonon frequency and polariza-

tion vector, respectively. The phonon dispersion and corresponding DOS from our simulations are shown in Fig. 9. As we observed from the panel (a) of the figure, the absence of imaginary frequencies confirms the dynamical stability of NdBiTe. The acoustic modes were found to be dominated by square-net of Bi, whereas the optical phonons have contributions mostly from Nd and Te ions. The observed relatively low frequency phonons, compared to ZrSiS/Se,^{32,50} could be attributed to the presence of heavy elements in NdBiTe. In panel (c) of the figure, we have shown the temperature dependence of the specific heat data, computed within the quasi-harmonic approximation.⁵¹ As can be observed from the figure, our calculated specific heat is consistent with our measurement in terms of trend, except an anomaly observed experimentally at 4.5 K. The values of γ and β extracted from the linear fit of specific heat data in the experimental temperature range (18 - 26 K) are 190 mJ/K² and 0.76 mJ/K⁴, respectively. And, θ_D calculated using γ and β is obtained as 197 K. The reason for the small discrepancy with experimental extracted values could be attributed to the missing magnetic contributions in our calculation, which are crucial in the vicinity of the transition temperature.

CONCLUSIONS

We have synthesized a polycrystalline NdBiTe by using the sealed tube method of solid-state reaction technique. From the temperature-dependent magnetic and specific heat measurements, we observed an antiferromagnetic configuration as the ground state of NdBiTe, with a Neel temperature of 4.5 K. The Neel temperature is observed to be less affected with the increase in magnetic field strengths, suggesting the robust nature of the phase transition. In the AFM state, the magnetic field-driven metamagnetic transition is observed from the isothermal magnetization data. The absence of short-range interactions is confirmed by our ac-susceptibility measurements, performed at various excitation frequencies. The extracted

γ , β , and θ_D parameters from specific heat data, suggest the presence of relatively stronger electronic correlations and weaker interatomic interactions in NdBiTe as compared to NdSbTe. Moreover, the transport studies infer the metallic nature with positive magnetoresistance. Consistent with our experimental results, our first-principles density functional theory based calculations predict an antiferromagnetic semimetallic nature of NdBiTe. Our simulations also indicate a weak topological nature associated with NdBiTe. The observed topological and magnetic characteristics from our work establish NdBiTe as a potential candidate for AFM-based spintronics applications.

ACKNOWLEDGMENTS

The authors acknowledge the Central Research Facility (CRF), IIT Delhi for the experimental facilities. We thank the MPMS3 facility of the Physics department, IIT Delhi for the ac-susceptibility measurements. AKG and BKM thanks SERB-DST (RP04583), Government of India for funding. PKM acknowledges the Council of Scientific & Industrial Research (CSIR), [09/086(1425)/2019-EMR-I] India for fellowship. BKM acknowledges the funding support from SERB, DST (CRG/2022/000178). The results presented in the paper are based on the computations using the High Performance Computing cluster, Padum, at the Indian Institute of Technology Delhi, New Delhi

Supporting Information Available

The supplementary information includes isothermal magnetization $M(H)$ plot and the first derivative of MR with respect to the applied field at various temperatures. It also consists of U-value calculation for Nd, utilized further in theoretical investigations.

References

- (1) Sankar, R.; Muthuselvam, I. P.; Rajagopal, K.; Ramesh Babu, K.; Murugan, G. S.; Bayikadi, K. S.; Mooven-daran, K.; Ting Wu, C.; Guo, G.-Y. Anisotropic Magnetic Properties of Non-symmorphic Semimetallic Single Crystal NdSbTe. *Cryst. Growth Des.* **2020**, *20*, 6585.
- (2) Pandey, K.; Basnet, R.; Wegner, A.; Acharya, G.; Nabi, M. R. U.; Liu, J.; Wang, J.; Takahashi, Y. K.; Da, B.; Hu, J. Electronic and magnetic properties of the topological semimetal candidate NdSbTe. *Phys. Rev. B* **2020**, *101*, 235161.
- (3) Chen, K.-W.; Lai, Y.; Chiu, Y.-C.; Steven, S.; Besara, T.; Graf, D.; Siegrist, T.; Albrecht-Schmitt, T. E.; Balicas, L.; Baumbach, R. E. Possible devil's staircase in the Kondo lattice CeSbSe. *Phys. Rev. B* **2017**, *96*, 014421.
- (4) Regmi, S.; Dhakal, G.; Kabeer, F. C.; Harrison, N.; Kabir, F.; Sakhya, A. P.; Gofryk, K.; Kaczorowski, D.; Oppeneer, P. M.; Neupane, M. Observation of multiple nodal lines in SmSbTe. *Phys. Rev. Mater.* **2022**, *6*, L031201.
- (5) Gao, F.; Huang, J.; Ren, W.; Li, M.; Wang, H.; Yang, T.; Li, B.; Zhang, Z. Magnetic and transport properties of the topological compound DySbTe. *Phys. Rev. B* **2022**, *105*, 214434.
- (6) Yang, M.; Qian, Y.; Yan, D.; Li, Y.; Song, Y.; Wang, Z.; Yi, C.; Feng, H. L.; Weng, H.; Shi, Y. Magnetic and electronic properties of a topological nodal line semimetal candidate: HoSbTe. *Phys. Rev. Materials* **2020**, *4*, 094203.
- (7) Schoop, L. M. et al. Tunable Weyl and Dirac states in the nonsymmorphic compound CeSbTe. *Science Advances* **2018**, *4*, 2317.
- (8) Neupane, M.; Belopolski, I.; Hosen, M. M.; Sanchez, D. S.; Sankar, R.;

- Szlawska, M.; Xu, S.-Y.; Dimitri, K.; Dhakal, N.; Maldonado, P.; Oppeneer, P. M.; Kaczorowski, D.; Chou, F.; Hasan, M. Z.; Durakiewicz, T. Observation of topological nodal fermion semimetal phase in ZrSiS. *Phys. Rev. B* **2016**, *93*, 201104.
- (9) Topp, A.; Lippmann, J. M.; Varykhalov, A.; Duppel, V.; Lotsch, B. V.; Ast, C. R.; Schoop, L. M. Non-symmorphic band degeneracy at the Fermi level in ZrSiTe. *New J. Phys.* **2016**, *18*, 125014.
- (10) Schoop, L. M.; Ali, M. N.; Straßer, C.; Topp, A.; Varykhalov, A.; Marchenko, D.; Duppel, V.; Parkin, S. S. P.; Lotsch, B. V.; Ast, C. R. Dirac cone protected by non-symmorphic symmetry and three-dimensional Dirac line node in ZrSiS. *Nat Commun* **2016**, *7*, 11696.
- (11) Fu, B.-B. et al. Dirac nodal surfaces and nodal lines in ZrSiS. *Sci. Adv.* **2019**, *5*, 6459.
- (12) Ali, M. N.; Schoop, L. M.; Garg, C.; Lippmann, J. M.; Lara, E.; Lotsch, B.; Parkin, S. S. P. Butterfly magnetoresistance, quasi-2D Dirac Fermi surface and topological phase transition in ZrSiS. *Sci. Adv.* **2016**, *2*, 1601742.
- (13) Singha, R.; Pariari, A. K.; Satpati, B.; Mandal, P. Large nonsaturating magnetoresistance and signature of nondegenerate Dirac nodes in ZrSiS. *Proc. Natl. Acad. Sci.* **2017**, *114*, 2468–2473.
- (14) Song, J.; Wang, J.; Wang, Y.; Zhang, L.; Song, M.; Li, Z.; Cao, L.; Liu, D.; Xiong, Y. Kohler’s rule and anisotropic Berry-phase effect in nodal-line semimetal ZrSiSe. *J. Appl. Phys.* **2022**, *131*, 065106.
- (15) Klemenz, S.; Hay, A. K.; Teicher, S. M. L.; Topp, A.; Cano, J.; Schoop, L. M. The Role of Delocalized Chemical Bonding in Square-Net-Based Topological Semimetals. *J. Am. Chem. Soc.* **2020**, *142*, 6350.
- (16) Klemenz, S.; Lei, S.; Schoop, L. M. Topological Semimetals in Square-Net Materials. *Annu. Rev. Mater. Res.* **2019**, *49*, 185.
- (17) Xu, Q.; Song, Z.; Nie, S.; Weng, H.; Fang, Z.; Dai, X. Two-dimensional oxide topological insulator with iron-pnictide superconductor LiFeAs structure. *Phys. Rev. B* **2015**, *92*, 205310.
- (18) Singha, R.; Pariari, A.; Satpati, B.; Mandal, P. Magnetotransport properties and evidence of a topological insulating state in LaSbTe. *Phys. Rev. B* **2017**, *96*, 245138.
- (19) Hosen, M. M.; Dhakal, G.; Dimitri, K.; Maldonado, P.; Aperis, A.; Kabir, F.; Sims, C.; Riseborough, P.; Oppeneer, P. M.; Kaczorowski, D.; Durakiewicz, T.; Neupane, M. Discovery of topological nodal-line fermionic phase in a magnetic material GdSbTe. *Sci Rep* **2018**, *8*, 13283.
- (20) Plokhikh, I.; Pomjakushin, V.; Gawryluk, D. J.; Zaharko, O.; Pomjakushina, E. Competing Magnetic Phases in LnSbTe (Ln = Ho and Tb). *Inorg. Chem.* **2022**, *61*, 11399.
- (21) Blöchl, P. E. Projector augmented-wave method. *Phys. Rev. B* **1994**, *50*, 17953–17979.
- (22) Kresse, G.; Joubert, D. From ultrasoft pseudopotentials to the projector augmented-wave method. *Phys. Rev. B* **1999**, *59*, 1758–1775.
- (23) Kresse, G.; Hafner, J. Ab initio molecular-dynamics simulation of the liquid-metal–amorphous-semiconductor transition in germanium. *Phys. Rev. B* **1994**, *49*, 14251–14269.
- (24) Kresse, G.; Furthmüller, J. Efficient iterative schemes for ab initio total-energy calculations using a plane-wave basis set. *Phys. Rev. B* **1996**, *54*, 11169–11186.

- (25) Perdew, J. P.; Burke, K.; Ernzerhof, M. Generalized Gradient Approximation Made Simple. *Phys. Rev. Lett.* **1996**, *77*, 3865–3868.
- (26) Dudarev, S. L.; Botton, G. A.; Savrasov, S. Y.; Humphreys, C. J.; Sutton, A. P. Electron-energy-loss spectra and the structural stability of nickel oxide: An LSDA+U study. *Phys. Rev. B* **1998**, *57*, 1505–1509.
- (27) Dudarev, S.; Manh, D. N.; Sutton, A. Effect of Mott-Hubbard correlations on the electronic structure and structural stability of uranium dioxide. *Philos. Mag. B* **1997**, *75*, 613–628.
- (28) Gebauer, P.; Poddig, H.; Corredor-Bohorquez, L. T.; Menshchikova, T. V.; Rusinov, I. P.; Golub, P.; Cagliaris, F.; Benndorf, C.; Lindemann, T.; Chulkov, E. V.; Wolter, A. U. B.; Büchner, B.; Doert, T.; Isaeva, A. Heavy-atom antiferromagnet gdbite: an interplay of magnetism and topology in a symmetry-protected topological semimetal. *Chem. Mater.* **2021**, *33*, 2420–2435.
- (29) Dove, M. T. *Introduction to Lattice Dynamics*; Cambridge Topics in Mineral Physics and Chemistry; Cambridge University Press, 1993.
- (30) Togo, A. First-principles phonon calculations with phonopy and phono3py. *J. Phys. Soc. Japan* **2023**, *92*, 012001.
- (31) Cucka, P.; Barrett, C. S. The crystal structure of Bi and of solid solutions of Pb, Sn, Sb and Te in Bi. *Acta Crystallographica* **1962**, *15*, 865–872.
- (32) Zhang, X.; Sun, S.; Lei, H. Massive fermions with low mobility in antiferromagnet orthorhombic CuMnAs single crystals. *Phys. Rev. B* **2017**, *96*, 235105.
- (33) Lv, B.; Chen, J.; Qiao, L.; Ma, J.; Yang, X.; Li, M.; Wang, M.; Tao, Q.; Xu, Z.-A. Magnetic and transport properties of low-carrier-density Kondo semimetal CeSbTe. *J. Condens. Matter Phys* **2019**, *31*, 355601.
- (34) Lei, S.; Duppel, V.; Lippmann, J. M.; Nuss, J.; Lotsch, B. V.; Schoop, L. M. Charge Density Waves and Magnetism in Topological Semimetal Candidates GdSb_xTe_{2-x-δ}. *Advan. Quantum Technol.* **2019**, *2*, 1900045.
- (35) Regmi, S.; Smith, R.; Sakhya, A. P.; Sprague, M.; Mondal, M. I.; Elius, I. B.; Valadez, N.; Ptok, A.; Kaczorowski, D.; Neupane, M. Observation of gapless nodal-line states in NdSbTe. *Phys. Rev. Mater.* **2023**, *7*, 044202.
- (36) Banerjee, B. On a generalised approach to first and second order magnetic transitions. *Phys. Lett.* **1964**, *12*, 16–17.
- (37) Pandey, K.; Saylor, L.; Basnet, R.; Sakon, J.; Wang, F.; Hu, J. Crystal Growth and Electronic Properties of LaSbSe. *Crystals* **2022**, *12*, 214434.
- (38) Salters, T. H.; Orlandi, F.; Berry, T.; Khoury, J. F.; Whittaker, E.; Manuel, P.; Schoop, L. M. Charge density wave-templated spin cycloid in topological semimetal NdSb_xTe_{2-x-δ}. *Phys. Rev. Mater.* **2023**, *7*, 044203.
- (39) Sankar, R.; Muthuselvam, I. P.; Babu, K. R.; Murugan, G. S.; Rajagopal, K.; Kumar, R.; Wu, T.-C.; Wen, C.-Y.; Lee, W.-L.; Guo, G.-Y.; Chou, F.-C. Crystal Growth and Magnetic Properties of Topological Nodal-Line Semimetal GdSbTe with Antiferromagnetic Spin Ordering. *Inorg. Chem.* **2019**, *58*, 11730.
- (40) Barua, S.; Hatnean, M. C.; Lees, M. R.; Balakrishnan, G. Signatures of the Kondo effect in VSe₂. *Scientific Reports* **2017**, *7*, 10964.
- (41) Li, C.; Boubeche, M.; Zeng, L.; Ji, Y.; Li, Q.; Guo, D.; Zhu, Q.; Zhong, D.;

- Luo, H.; Wang, H. Electron–Electron Interaction and Weak Antilocalization Effect in a Transition Metal Dichalcogenide Superconductor. *physica status solidi (RRL)* **2022**, *16*, 2100650.
- (42) Pandey, K. et al. Magnetic Topological Semimetal Phase with Electronic Correlation Enhancement in SmSbTe. *Adv. Quantum Technol.* **2021**, *4*, 2100063.
- (43) Hu, J.; Tang, Z.; Liu, J.; Liu, X.; Zhu, Y.; Graf, D.; Myhro, K.; Tran, S.; Lau, C. N.; Wei, J.; Mao, Z. Evidence of Topological Nodal-Line Fermions in ZrSiSe and ZrSiTe. *Phys. Rev. Lett.* **2016**, *117*, 016602.
- (44) Jayakumar, A.; Dixit, V.; Jose, S.; Kamble, V. B.; Jaiswal-Nagar, D. Charge transport variation from Bloch–Grüneisen to Mott variable range hopping and transport change due to hydrogenation in Palladium thin films. *Sci. Rep.* **2021**, *11*, 22298.
- (45) Stampfl, C.; Van de Walle, C. G. Density-functional calculations for III-V nitrides using the local-density approximation and the generalized gradient approximation. *Phys. Rev. B* **1999**, *59*, 5521–5535.
- (46) Su, C.-C.; Li, C.-S.; Wang, T.-C.; Guan, S.-Y.; Sankar, R.; Chou, F.; Chang, C.-S.; Lee, W.-L.; Guo, G.-Y.; Chuang, T.-M. Surface termination dependent quasiparticle scattering interference and magneto-transport study on ZrSiS. *New J. Phys.* **2018**, *20*, 103025.
- (47) Weiland, A.; Chaparro, D. G.; Vergniory, M. G.; Derunova, E.; Yoon, J.; Oswald, I. W. H.; McCandless, G. T.; Ali, M.; Chan, J. Y. Band structure engineering of chemically tunable LnSbTe (Ln = La, Ce, Pr). *APL Mater.* **2019**, *7*, 101113.
- (48) Lei, S. et al. Band Engineering of Dirac Semimetals Using Charge Density Waves. *Adv. Mater.* **2021**, *33*, 2101591.
- (49) Togo, A.; Tanaka, I. First principles phonon calculations in materials science. *Scr. Mater.* **2015**, *108*, 1–5.
- (50) Singha, R.; Samanta, S.; Chatterjee, S.; Pariari, A.; Majumdar, D.; Satpati, B.; Wang, L.; Singha, A.; Mandal, P. Probing lattice dynamics and electron-phonon coupling in the topological nodal-line semimetal ZrSiS. *Phys. Rev. B* **2018**, *97*, 094112.
- (51) Baroni, S.; Giannozzi, P.; Isaev, E. Density-functional perturbation theory for quasi-harmonic calculations. *Rev Mineral Geochem* **2010**, *71*, 39–57.

TOC Graphic

